ISSN 1616-7341, Volume 60, Number 3

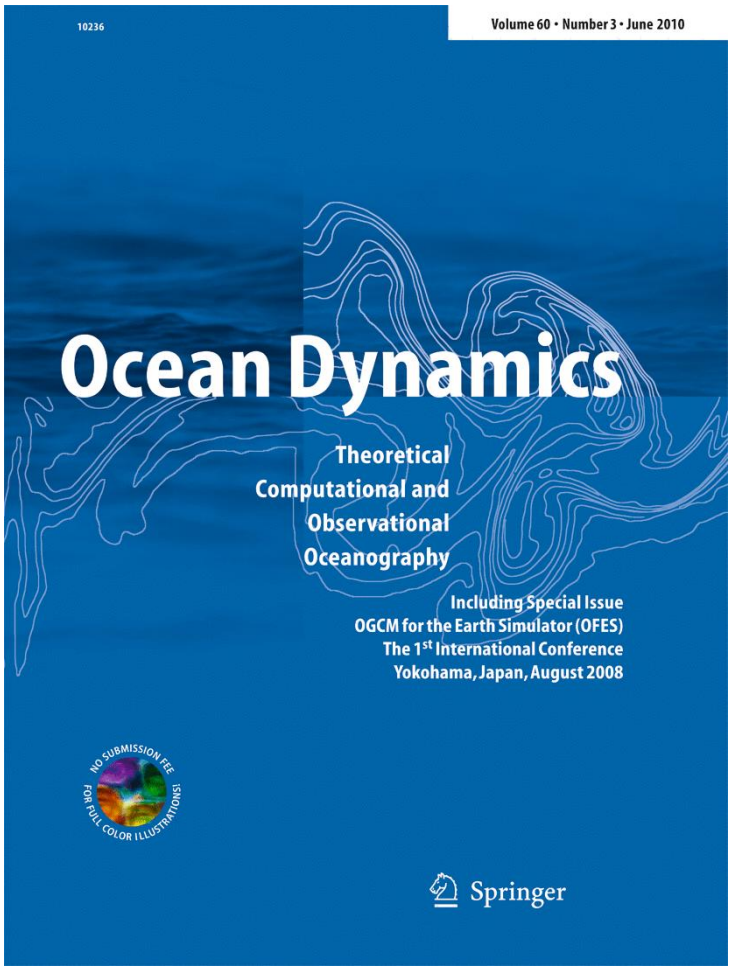

Ocean Dynamics (2010) 60:673–691
DOI 10.1007/s10236-010-0295-1

Decadal variability of the Kuroshio Extension: mesoscale eddies and recirculations

Bunmei Taguchi · Bo Qiu · Masami Nonaka · Hideharu Sasaki · Shang-Ping Xie · Niklas Schneider

Received: 13 July 2009 / Accepted: 21 April 2010 / Published online: 16 May 2010

Abstract An eddy-resolving multidecadal ocean model hindcast simulation is analyzed to investigate time-varying signals of the two recirculation gyres present respectively to the north and south of the Kuroshio Extension (KE) jet. The northern recirculation gyre (NRG), which has been detected at middepth recently by profiling float and moored current meter observations, is a major focus of the present study. Low-frequency variations in the intensity of the recirculation gyres are overall highly correlated with decadal variations of the KE jet induced by the basin-wide wind change. Modulation of the simulated mesoscale eddies and its relationship with the time-varying recirculation gyres are also evaluated. The simulated eddy kinetic energy in the upstream KE region is inversely correlated with the intensity of the NRG, consistent with previous observational studies. Eddy influence on the low-frequency modulation of the NRG intensity at middepth is further examined by a composite analysis of turbulent Sverdrup balance, assuming a potential vorticity balance between the mean advection and the convergent eddy fluxes during the different states of the recirculation gyre. The change in the NRG intensity is adequately explained by that inferred by the turbulent Sverdrup balance, suggesting that the eddy feedback triggers the low-frequency modulation of the NRG intensity at middepth.

Keywords Kuroshio Extension · Recirculation gyres · Mesoscale eddies · High-resolution ocean model

Responsible Editor: Yukio Masumoto

B. Taguchi (✉) · H. Sasaki
Earth Simulator Center, Japan Marine-Earth Science and Technology, 3173-25 Showa-machi, Kanazawa-Ku, Yokohama, Kanagawa 236-0001, Japan
e-mail: bunmei@jamstec.go.jp

B. Qiu
Department of Oceanography, University of Hawaii at Manoa, 1000 Pope Rd., Honolulu, HI 96822, USA

M. Nonaka
Research Institute for Global Change, Japan Marine-Earth Science and Technology, 3173-25 Showa-machi, Kanazawa-Ku, Yokohama, Kanagawa 236-0001, Japan

S.-P. Xie · N. Schneider
International Pacific Research Center, University of Hawaii at Manoa, 1680 East-West Rd., Honolulu, HI 96822, USA

1 Introduction

The Kuroshio Extension (KE) region east of Japan is one of the major action centers of decadal variability in the extratropical North Pacific climate (Schneider and Cornuelle 2005; Qiu et al. 2007; Kwon and Deser 2007). Studies have demonstrated that the large-scale pattern and its phase change in sea surface height (SSH) in the KE region can be adequately explained by baroclinic Rossby waves forced by basin-scale wind change (Miller et al. 1998; Deser et al. 1999; Seager et al. 2001; Schneider and Miller 2001; Qiu 2003; Kwon and Deser 2007; Ceballos et al. 2009). Despite its usefulness, the Rossby wave dynamics fails to account for frontal-scale patterns of the SSH variability (Taguchi et al. 2007), which has a direct relevance to ecosystem variability (Sasai et al. 2007, 2010) and ocean front–atmosphere interaction in the region (Nakamura et al. 2004; Tokinaga et al. 2009; Taguchi et al. 2009). Analyses of high-resolution ocean general circulation model

(OGCM) experiments have suggested that adjustment of the KE's recirculation gyres organize the incoming large-scale Rossby wave signals into narrow oceanic fronts (Taguchi et al. 2005, 2007).

An anticyclonic recirculation gyre (RG) exists on the southern flank of the KE outflow east of Japan (e.g. Niiler et al. 2003a, b). This southern RG (SRG) is often thought of as an inertial circulation driven by advection of low potential vorticity (PV) anomalies from the south along the western boundary (Cessi et al. 1987; Hogg et al. 2005). The SRG has been well recognized as an inseparable component of the KE system; the link among variations of the SRG strength, the location and strength of the KE path, and the regional mesoscale eddy activity is well established from satellite altimeter observations (Qiu and Chen 2005, 2010). On the other hand, it was not until recently that the *time-mean* RG to the north of the KE jet (northern RG, NRG) was found to exist at middepth (~1,500 m) in profiling float and moored current meter measurements (Qiu et al. 2008; Jayne et al. 2009). Regarding the role played by the RGs in the variability of western boundary currents (WBCs), previous idealized model studies have highlighted self-sustained low-frequency oscillations originated from intrinsic variability of the WBC's RGs (Jiang et al. 1995; Dijkstra and Ghil 2005; Pierini et al. 2009) and the importance of eddy forcing for the generation of intrinsic variability of the RGs (Berloff et al. 2007). This view of the low-frequency internal variability conflicts with the deterministic view of the low-frequency variability of the KE system responding to the external wind forcing through the linear Rossby wave adjustment.

Such interplay between the oceanic internal variability and the time-varying wind forcing (see also Pierini and Dijkstra 2009 for a review) has recently been simulated by eddy-resolving ocean model runs that are long enough to capture the low-frequency variability of WBCs. At a horizontal resolution of 0.1°, the multidecadal (currently 59 years) simulations of OGCM for the Earth Simulator (OFES) have provided unique datasets to study the low-frequency variability of frontal- and mesoscale features in the ocean (Masumoto et al. 2004; Sasaki et al. 2008). An intrinsically generated decadal variability of the KE jet and its recirculations was manifested in one of the OFES integrations, forced with climatological atmospheric forcing. Another integration, forced with surface atmospheric variables from a reanalysis product, suggested that the temporal phase change of the KE's internal variation is synchronized with the large-scale oceanic Rossby wave adjustment to wind change (Taguchi et al. 2007). Qiu et al. (2008) also analyzed this integration and demonstrated that the time-mean NRG in the KE system is driven by forcing exerted by mesoscale eddies.

From the view point of the recirculation adjustment to the large-scale circulation changes carried by wind-forced Rossby waves, it is of great interest to clarify how the KE's RGs modulate on decadal time scale and how this modulation is related to the wind and eddy forcings. The OFES hindcast simulation allows us to examine the multidecadal evolution of the subsurface field where the signal of the KE's NRG is most prominent and the interannual-to-decadal modulations of the mesoscale eddy activity/forcing. The present study has three goals. The first is to describe the time-varying signals of the KE's RGs (Section 3). The second goal is to evaluate modulations of mesoscale eddies associated with the intensity change in the KE's NRG and wind-forced large-scale circulation changes (Section 4). Finally, the third goal is to relate the time-varying signals of the RGs to the modulation of the eddy forcing (Section 5). The rest of the paper is organized as follows: Section 2 describes model and observational data used in this study. Sections 3–5 present results corresponding to the three research goals mentioned above, respectively. Section 6 summarizes the results and discusses their implications.

2 Model and observation

We analyze a multidecadal hindcast by the OGCM for the Earth Simulator (OFES; Masumoto et al. 2004; Sasaki et al. 2008). The OFES is based on the modular ocean model (MOM3; Pacanowski and Griffies 2000) and has been substantially modified for optimal performance on the Earth Simulator. The model covers a near-global domain extending from 75° S to 75° N, with horizontal resolution of 0.1° and 54 vertical levels. It is forced by surface wind stress, heat, and freshwater fluxes derived from the daily-mean National Centers for Environmental Prediction (NCEP) and National Center for Atmospheric Research (NCAR) reanalysis (Kalnay and coauthors 1996). Surface turbulent heat flux is calculated using the bulk formula with the model SST, meteorological variables from the NCEP/NCAR atmospheric reanalysis, and a constant exchange coefficient as in Rosati and Miyakoda (1988), while sea surface salinity is restored to the observed monthly climatology. From an initial condition at rest with observed annual-mean temperature and salinity, the model was first spun up for 50 years with monthly climatological atmospheric forcing, followed by a 58-year hindcast integration forced with the daily-mean

reanalysis data from 1950 to 2007. More detailed descriptions on the model configurations are provided in Nonaka et al. (2006) and Sasaki et al. (2008). Resolving fronts and eddies from the tropics to midlatitudes in the world ocean, this multidecadal hindcast integration has been providing a unique opportunity to study interannual-to-decadal variability of narrow WBCs and their eastward extensions (Nonaka et al. 2006, 2008; Taguchi et al. 2007). In this study, we analyze monthly and three daily outputs from the hindcast simulation, the latter of which enables us to investigate interannual-to-decadal modulation of the mesoscale eddy activity and forcing.

The OFES hindcast is compared to the following observational data. We use sea surface height anomaly maps compiled from TOPEX/POSEIDON, JASON and ERS-1/2 altimeter measurements and distributed by AVISO (hereafter referred to simply as altimeter observation; Ducet et al. 2000). The data are mapped on the Mercator grid with 1/3° resolution in longitude and varying spacing in latitude (from 37 km at the equator to 18.5 km at 60° N). Weekly mean data that cover a 15-year period from January 1993 to December 2007 are used. For the observed mean SSH fields, we use the 1992–2002 mean dynamic ocean topography that is calculated using jointly data of satellite altimetry, near-surface drifters, NCEP wind, and GRACE (Niiler et al. 2003a; Maximenko and Niiler 2004).

3 Modulations of the KE's recirculation gyres

In this section, we first examine time-varying signals of the KE's recirculation gyres from the OFES hindcast simulation and compare them with dominant modes of the KE jet variability. To define the properties of the recirculation gyres, it is useful to remark on different vertical structures of two RGs, readily seen in the simulated long-term mean fields at the surface and at middepth (Fig. 1). The anticyclonic SRG is prominent both in the mean SSH (Fig. 1a) and the mean depth of the $27.6\sigma_\theta$ isopycnal (Fig. 1b). The SRG is located to the south of the simulated KE jet that flows eastward along about 35° N as observed, whereas the cyclonic NRG, situated to the north of the KE, is clearly visible only in the isopycnal depth at middepth, although there is a corresponding trough at the surface. To describe the NRG properties in the present study, we focus on the isopycnal surface of $27.6\sigma_\theta$, which is placed at nearly the same depth as the $27.575\sigma_\theta$ isopycnal surface employed by Qiu et al. (2008). Note that the existence of the simulated NRG is robust in the 48-year-long OFES climatology.

Temporal variations of both the RGs are closely related to the KE jet variability. As reference indices of the latter, we employ two leading principal components (PCs) of the zonal mean SSH averaged over the KE region (140–180° E) within 30–45° N (Fig. 2d, e, green curves). Taguchi et al. (2007) have shown that the first EOF mode represents the latitudinal shift of the front with a single peak in SSH (Fig. 2a, black curve) and a dipole in the associated zonal current (Fig. 2b, black curve) centered around the mean KE jet location (35.8° N, Fig. 2c), whereas the second mode represents the intensity change of the jet with a peak in the zonal current (Fig. 2b, red curve) at the latitude of the mean jet. They have also shown that a linear Rossby wave model forced by observed wind successfully reproduces the time series of these EOF modes, suggesting that the wind-forced Rossby waves with a broad meridional scale trigger frontal-scale adjustments upon arriving in the KE region. Based on their finding, we use the time series of the zonal mean SSH EOFs as indices of the large-scale wind-forced Rossby waves as well.

Following Qiu and Chen (2005), the KE's southern recirculation intensity $S(t)$ is defined as

$$S(t) = \int\int_{\mathrm{ssh}>\mathrm{ssh}_0} \mathrm{ssh}(x, y, t)dxdy \tag{1}$$

where $\mathrm{ssh}(x, y, t)$ is the monthly mean absolute SSH and $\mathrm{ssh} > \mathrm{ssh}_0$ denotes the area within which the SSH value exceeds a threshold ssh_0 (chosen to be 90 cm) in the upstream KE region (30–37° N, 141–158° E). Similarly, the northern recirculation intensity $N(t)$ is defined as

$$N(t) = -\int\int_{h'<h'_0} h'(x, y, t)dxdy \tag{2}$$

where $h'(x, y, t)$ is the spatial anomaly of the isopycnal depth of $27.6\sigma_\theta$ from the mean depth averaged over the KE region (25–45° N, 140–165° E) and $h' < h'_0$ denotes the area within which the depth anomaly is shallower than a threshold h'_0 (chosen to be −150 m) in the upstream KE region (30–40° N, 141–158° E). The latitudinal position of the recirculations, y_S and y_N for the SRG and NRG, respectively, is also defined by the weighted average of the latitudinal center of the recirculations y:

$$y_S(t) = \frac{1}{S(t)}\int\int_{\mathrm{ssh}>\mathrm{ssh}_0} y \times \mathrm{ssh}(x, y, t)dxdy \tag{3}$$

$$y_N(t) = -\frac{1}{N(t)}\int\int_{h'<h'_0} y \times h'(x, y, t)dxdy \tag{4}$$

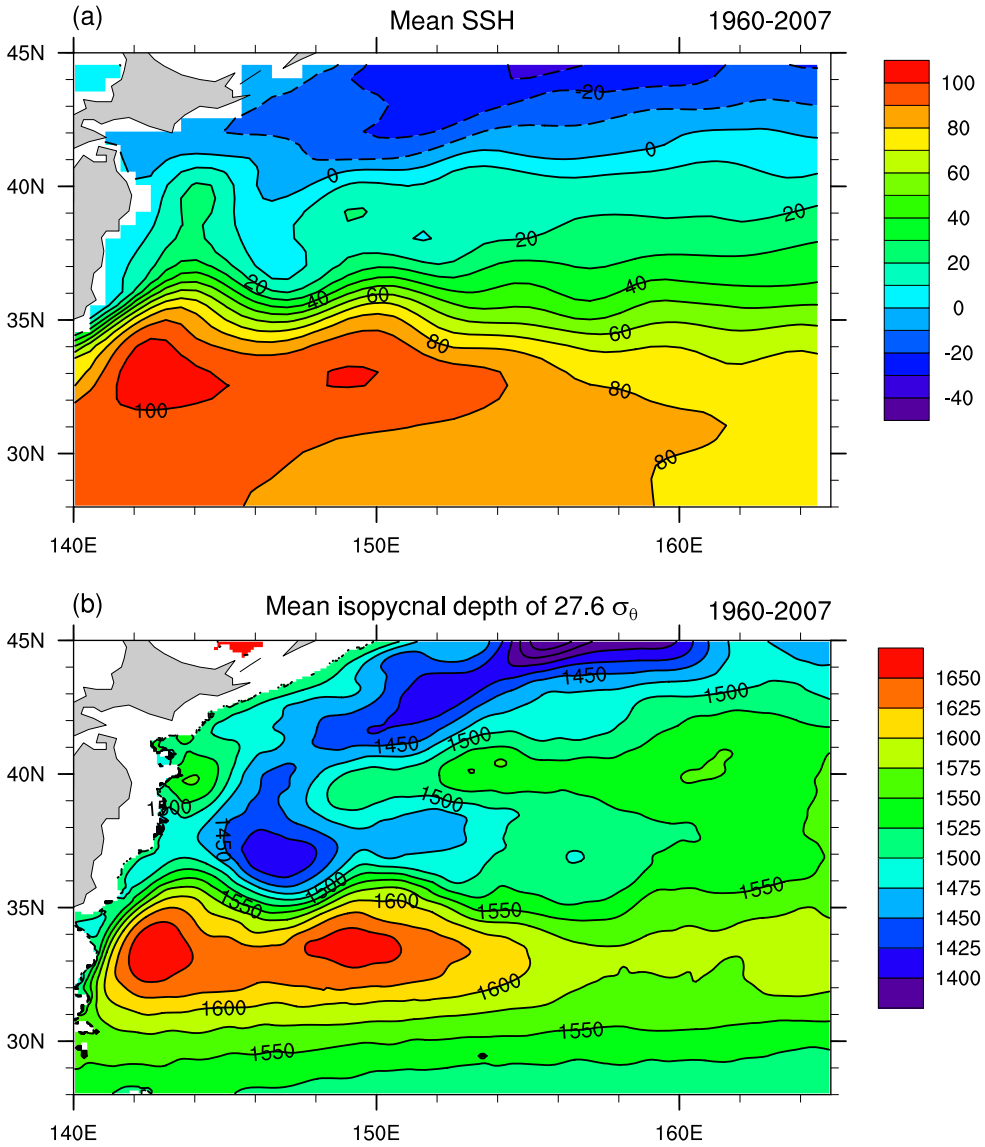

Fig. 1 Long-term mean fields of simulated **a** SSH and **b** isopycnal depth of 27.6σ_θ, averaged over the period from 1960 to 2007 in the KE region. Contour intervals are 10 cm for SSH and 25 m for the isopycnal depth

Choice of the thresholds to define the RGs has little effect on the results described below. In the following sections, we first describe the characteristics of the recirculation time series (the latitudinal position and intensity) and their relations with the indices of the KE jet variability. Based on these temporal characteristics, we further discuss the spatial patterns of the time-varying middepth circulations between two 25-year epochs prior and after 1980 and those associated with the variations in NRG intensity after 1980.

3.1 Temporal characteristics

Figure 2d shows the time series of the SRG and NRG positions, along with the first PC of the zonal mean SSH in the KE region (SSH-PC1) which mainly represents the meridional migration of the KE jet. The SSH-PC1 time series displays a distinct decline as much as three standard deviations in PC1, equivalent to a southward shift by ~1.2° during the early 1980s (see also Fig. 4 in Taguchi et al. 2007). This decline is likely a delayed response to the wind change associated with the 1976/1977 regime shift (Miller et al. 1998). The latitudinal positions of both the RGs closely follow the SSH-PC1 decline, suggesting the whole KE system responded to the wind forcing change.

Low-frequency intensity variations of both the NRG and SRG are overall well correlated with the time series of the second PC (SSH-PC2) which represents the intensity change of the KE jet as shown in Fig. 2e. This indicates again that the recirculation intensities are primarily controlled by wind-forced large-scale

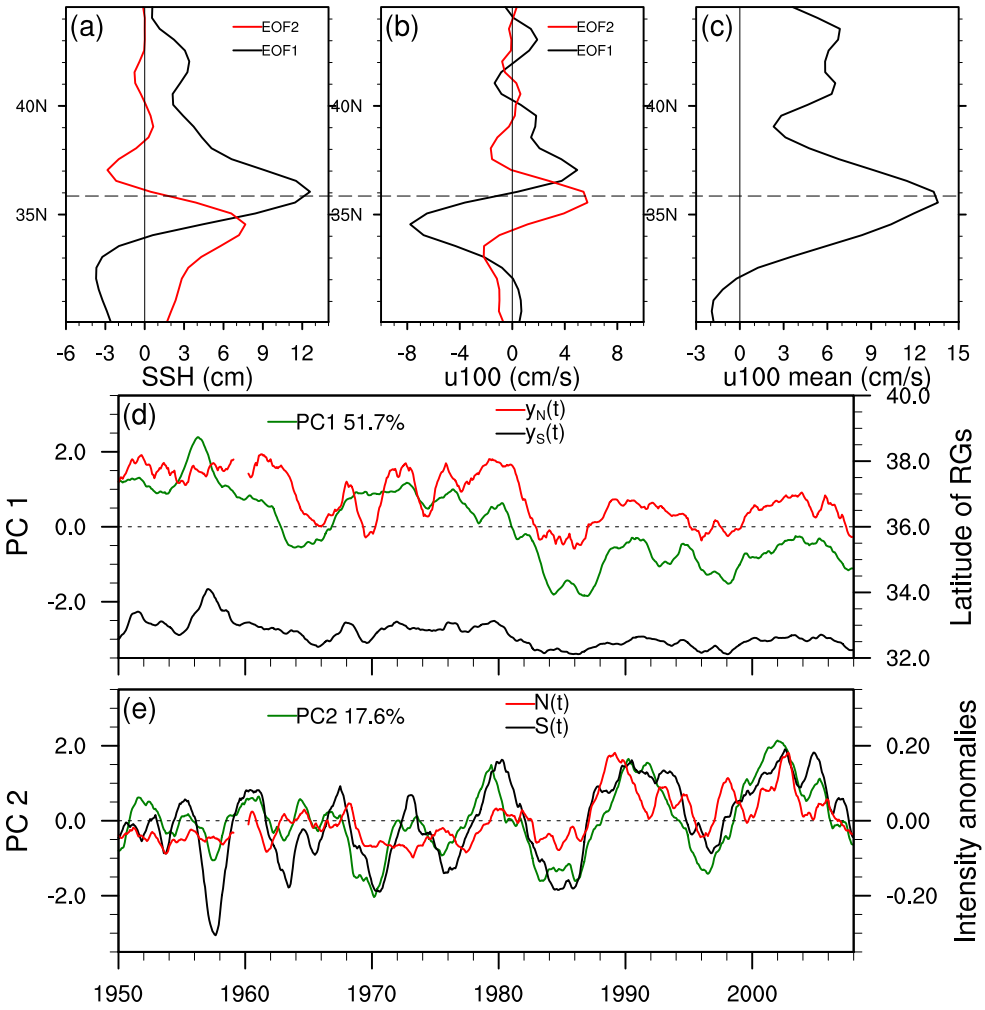

Fig. 2 **a** The two leading EOFs of zonal and monthly mean SSH anomalies (centimeters) for the OFES multidecadal (1950–2007) hindcast. *Black (red) curve* represents the first (second) mode. **b** Zonal current velocity at 100 m depth (centimeters per second) projected onto the PCs of the zonal mean SSH anomalies in the OFES hindcast. **c** OFES climatology of zonal current velocity at 100 m depth for the period 1950–2007. **d** The first PC (*PC1*) of the zonal mean SSH anomalies (normalized to unit standard deviation, *green curve*), the latitudinal position of the NRG ($y_N(t)$; *red curve*; axis on the *right*), and that of the SRG ($y_S(t)$; *black curve*) in the OFES hindcast. **e** The second PC (*PC2*; *green*), intensity anomalies of the NRG ($N(t)$; *red curve*; axis on the *right*; units in 10^{15} m^3), and that of the SRG ($S(t)$; *black curve*; units in 10^{12} m^3). Seasonal cycles are removed from all the time series in **d** and **e** by subtracting their climatological monthly mean and further applying a 13-month running mean filter

circulation. At a closer look, however, the correlation of the NRG intensity with the SSH-PC2 (0.58) is lower than that of the SRG intensity (0.80). The difference between the two correlations arises from two factors. First, the time series of the two recirculations are not perfectly correlated with each other; the SRG intensity exhibits variations of slower timescale than the NRG intensity and is better correlated with the decadal SSH-PC2, indicating that mechanisms for the modulation of the two RGs are different. The SRG, which is most prominent in the ocean subsurface shallower than the thermocline, is more directly connected with the wind-forced subtropical gyre, whereas the middepth NRG is influenced by eddies that are rather stochastic in the OFES simulation and not necessarily in direct link to the wind. Second, the lower correlation between the NRG strength and SSH-PC2 also appears to be due to weak prior to 1980 (Fig. 2e).

It is worth mentioning that there is an increasing trend in the simulated SRG and NRG intensity. To examine the cause of this, we look into Ekman pumping velocity w_e based on NCEP/NCAR reanalysis wind stress that is used to force the OFES hindcast:

$$w_e = \mathrm{curl}\left(\frac{\boldsymbol{\tau}}{f\rho_0}\right) \tag{5}$$

where $\boldsymbol{\tau}$ is the wind stress vector, f the Coriolis parameter, and ρ_0 the reference water density. We apply an EOF analysis to annual mean field of w_e within the North Pacific domain and find that the time series of the first EOF, which explains 13.2% of the total variance, exhibits an increasing trend (Fig. 3b). The associated spatial pattern is characterized by a basin-wide meridional dipole with a positive w_e to the north of about 38° N and a negative one to the south (Fig. 3a). Thus, the w_e component contributed by its first EOF mode tends to drive monotonically large-scale subpolar and subtropical gyre circulations. The zonal mean of total w_e averaged over a longitudinal sector (150° E–150° W) provides a proxy of the geostrophic stream

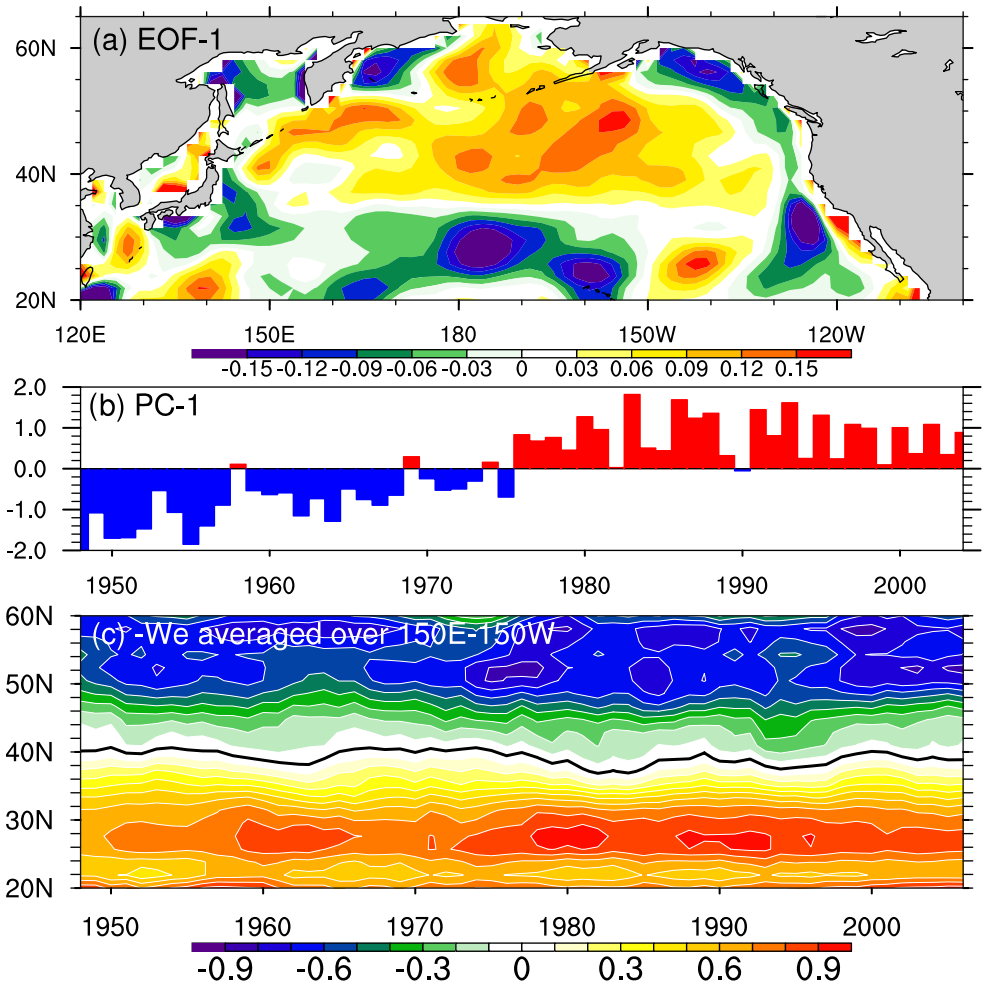

Fig. 3 **a** The first EOF pattern of the annual mean Ekman pumping velocity (unit is $\times 10^{-5}$ m s^{-1}) based on NCEP/NCAR reanalysis wind stress. **b** The first PC (normalized to unit standard deviation) of the annual mean Ekman pumping velocity. **c** Latitude-time section of the zonal mean Ekman pumping velocity averaged over a zonal sector (150° E–150° W, unit in $\times 10^{-5}$m s^{-1}). The sign is flipped so that the positive (negative) value indicates an anti-cyclonic (cyclonic) stream function.

function at 150° E by Sverdrup dynamics (e.g., Pedlosky 1996). A latitude-time section of this "stream function", indeed, displays a gradual spin-up of the subtropical and subpolar gyre circulations with an increasing maximum value around 28° N and an decreasing minimum value around 52° N, respectively (Fig. 3c). This large-scale gyre spin-up can intensify the RG intensity via nonlinear adjustments (e.g., Taguchi et al. 2005), which is presumably the cause for the increasing trend in the simulated recirculation intensity.

3.2 Changes between two epochs across 1980

The lower correlation between the NRG intensity and the SSH-PC2 reflects the weak interannual variability of the NRG intensity before 1980, as well as its less pronounced interannual-to-decadal variability than the SSH-PC2 after 1980. The former one may be related to the fact that the KE jet had a northerly position before 1980 (Fig. 2d, green curve). As shown in Fig. 6 of Qiu et al. (2008), the KE jet wandered around 37° N prior to 1980, as compared to 35° N after 1980, whereas the eastward-flowing subarctic front remained near 40° N. More closely aligned KE and the subarctic front prior to 1980 left less space for the NRG to develop and may have led to its weakened variability.

To examine the spatial patterns of the KE jet and RGs for the contrasting two epochs across 1980, the epoch average maps of PV (shade) and stream functions (contours) on the isopycnal depth of 27.6σ_θ are constructed for the 25-year epoch after 1980 (1981–2005), that before 1980 (1956–1980), and their difference (Fig. 4a–c). The PV is defined as

$$Q = \frac{f+\zeta}{\rho}\frac{\partial \rho}{\partial z} \tag{6}$$

where f is Coriolis parameter, ζ the vertical component of the relative vorticity, and ρ the potential density. The stream function composite for the epoch after 1980

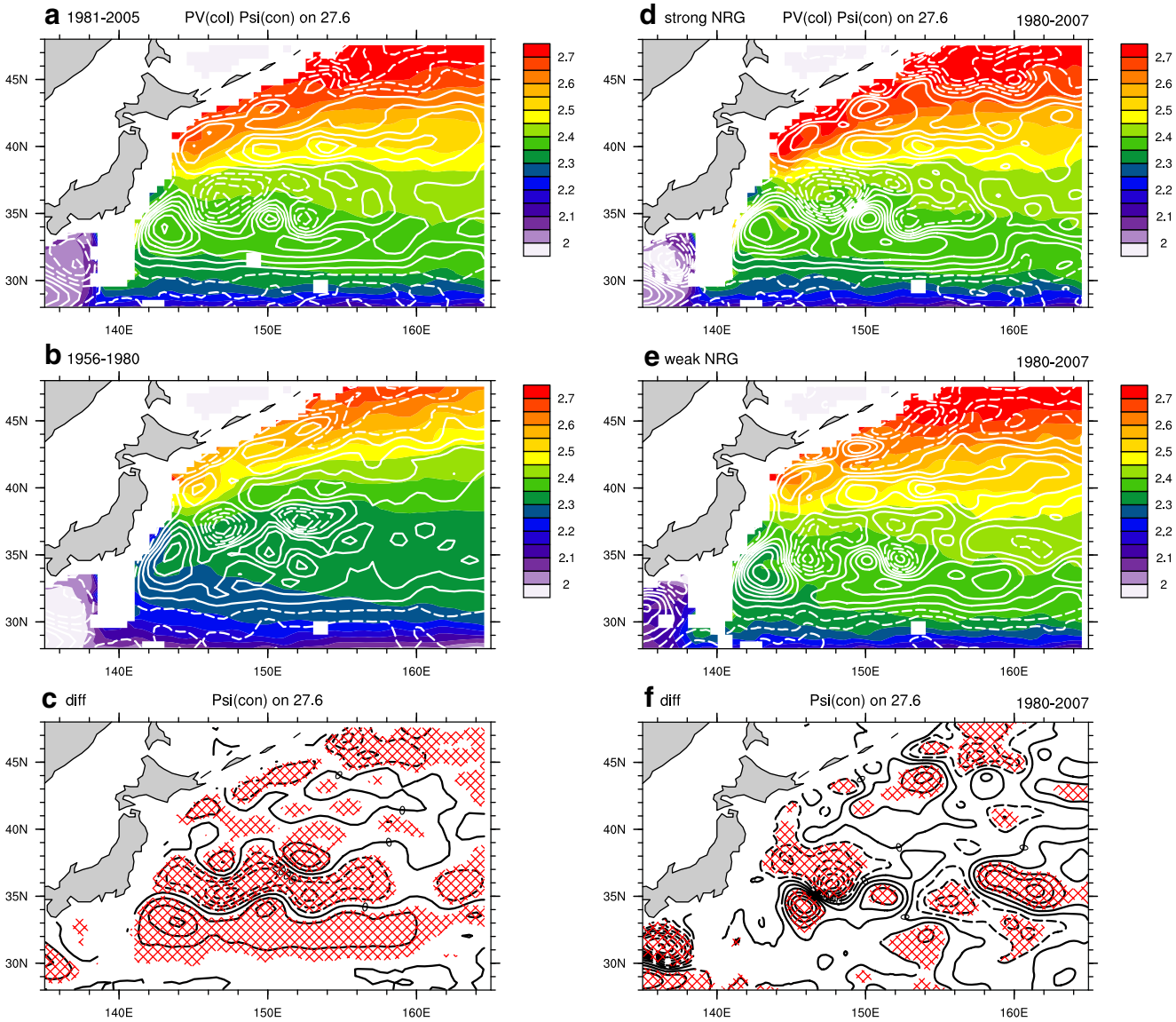

Fig. 4 Epoch averages of the potential vorticity (*shade*) and the stream function (*contours*) on the isopycnal of 27.6σ_θ for the period of **a** 1981–2005, **b** 1956–2005, and **c** their difference in the stream function. **d**–**f** Same as **a**–**c** but composite maps during the period 1980–2007 when the NRG intensity is **d** stronger, **e** weaker than its one standard deviation, and their difference. Data points in time series of the NRG intensity sampled for the composite are indicated with orange and purple dots in Fig. 7. Statistical significance for the stream function difference is indicated with red hatching in **c** and **f**. The signals hatched by *slanted red crossed lines* are statistically siginificant at 95% confidence level

(white contours in Fig. 4a) displays strong and spatially expanded NRG associated with the southward shift of the KE path after 1980. The difference pattern, which is statistically siginificant at 95% confidence level based on the two-sided Student' *t* test (red hatched in Fig. 4c), is similar to the epoch difference of SSH associated with the KE's meridional shift (Fig. 8e of Taguchi et al. 2007) and is presumably initiated by the basin-scale wind change associated with the 1976 climate shift. The intensification of the NRG in the latter epoch compared to the former is also partly due to the increasing trend in the NRG intensity caused by the basin-scale wind stress curl trend as mentioned in the previous subsection.

The PV composite for each epoch (color shade in Fig. 4a, b) exhibits a spatial pattern similar to the mean quasigeostrophic PV distribution averaged over the period 2000–2004 shown by Qiu et al. (2008). The PV gradually increases with latitude, while its latitudinal gradient is reduced in the vicinity of the KE jet.

Thus, there is no distinct frontal feature in PV on the isopycnal of 27.6σ_θ, which is often seen in shallower isopycnals (Talley 1988).

3.3 Low-frequency variations of RGs' intensity after 1980

Interannual-to-decadal variations of the RGs as well as SSH-PC2 became more prominent during the epoch after 1980 than the epoch before (Fig. 2e). To examine the spatial pattern with respect to the NRG intensity, composite maps during the latter (after 1980) epoch are constructed. Strong and weak NRG phases are defined based on the time series of the NRG intensity: The strong phase when the NRG intensity is above its one standard deviation and the weak phase below the minus one standard deviation. Data points in the NRG intensity time series sampled for the composite are indicated with orange and purple dots in Fig. 7c. The composite maps of the stream function with respect to the NRG intensity (Fig. 4d, e) captures the contrast in spatial patterns of the KE jet and RGs. In its strong phase, the well-defined middepth NRG is discernibly centered around 37° N, 147.5° E to the north of the KE jet, while the amplitude and the spatial extent of the NRG are substantially reduced during its weak phase. Furthermore, the KE's quasistationary meanders, which consist of zonally aligned cyclonic and anticyclonic circulations, are more contracted in zonal direction during the weak NRG phase, reminiscent of bimodal (elongated and contracted) modes of the KE jet as described in Qiu (2002).

4 Modulations of mesoscale eddy activity

Satellite altimeter observations have revealed that the mesoscale eddy activity and RGs exhibit distinct decadal modulations in the KE region (Qiu and Chen 2005, 2010). The multidecadal OFES hindcast simulation provides an unique opportunity to further elucidate mechanisms responsible for the decadal modulations of eddies and its possible influence on the RG variabilities. Thus, it is important to examine the degree to which OFES can simulate the mesoscale eddy modulations. In the following subsections, we first compare the simulated mesoscale eddy variability with that observed by altimeters. Then we discuss the simulated relationship between the modulations of the eddies and recirculations. Finally, the relationship between the eddy modulations and wind-forced large-scale circulations is discussed.

4.1 Comparison between simulated and observed modulations

Time series of the eddy activity at the surface averaged over the upstream (32–38° N, 141–155° E) and downstream (32–38° N, 160–180° E) KE regions are compared between the OFES simulation and satellite altimeter observations (Fig. 5). The upstream region corresponds to a region where the RGs are distinct (see Fig. 1), while the downstream region extends roughly from the Shatsky Rise to the International Date Line (see Fig. 1b of Qiu and Chen 2010). The eddy activity is measured by the eddy kinetic energy (EKE) defined as $\mathrm{EKE} = 1/2\left(u_g'^2 + v_g'^2\right)$ where u_g' and v_g' are respectively zonal and meridional surface geostrophic current velocity components that are high-pass filtered with a half power cutoff period of 300 days. The geostrophic current velocity components are computed based on three daily snap shots of SSH anomalies (SSHA) for the OFES and weekly mean merged SSHA for the altimeter.

In the upstream KE region, the simulated EKE time series do not agree well with the observed on their phase evolution due to the nonlinear and stochastic nature of simulated eddies (Fig. 5a). On the other hand, the EKE's phase evolution is better simulated in the downstream KE region, especially its low-frequency modulations except the too high EKE level around 2002 (Fig. 5b). The discrepancy between the model and the observations points to the remaining difficulty for many eddy-resolving ocean models in simulating accurately the mean level of the eddy activity (McClean et al. 2009) and its modulations. Despite such difficulty, however, it is still useful to examine the simulated EKE change since densely sampled subsurface observations, such as those from the ARGO floats, have not been obtained for a period long enough to study the low-frequency variability of the RGs and its relation to eddies. The hope is that a solid understanding of the eddy variability and its effect will be achieved when more observations become available.

Focusing on the contrast between the KE's bimodal states[1] rather than its phase transitions, we further compare the spatial patterns of the simulated and the observed EKE fields. Figure 6 shows the composite maps of square root of EKEs (color shade) based

[1]Hereafter "bimodal states" are referred to as two contrasting states of the KE system with respect to the NRG intensity, KE's quasistationary meanders (Section 3.3), and EKE level in the upstream KE region (discussed in this section).

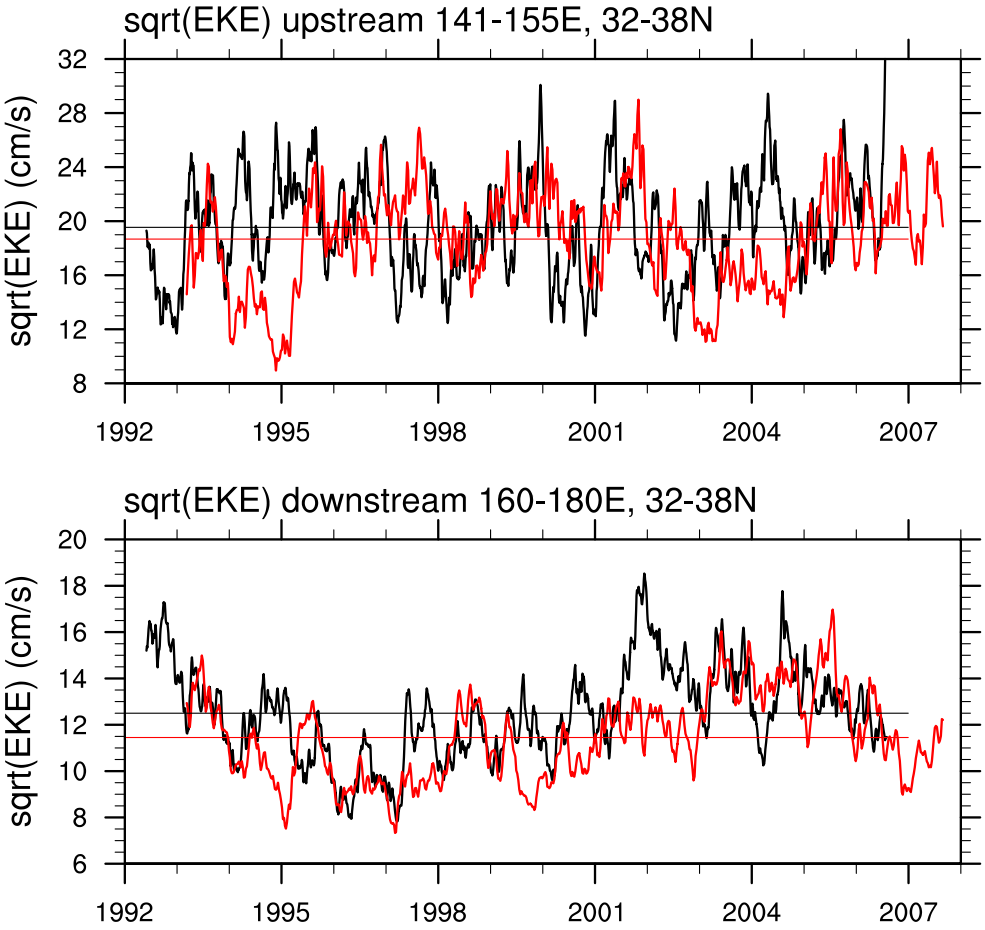

Fig. 5 Time series of regionally averaged square root of EKE in the upstream KE region (*top*; 32–38° N, 141–155° E) and downstream KE region (*bottom;* 32–38°N, 160–180° E). *Black curves* indicate EKEs from the OFES hindcast simulation based on three daily SSH anomalies while *red curves* from the altimeter observation based on weekly SSH anomalies. Mean value of the square root of the EKEs during the comparison period (1992–2007) are shown with *horizontal reference line*. Units are in centimeters per second

on the simulated NRG strength during the period of altimeter observations (1992–2005) along with the mean SSH (contours). Note that the surface expression of the NRG is discernible around 37° N, 147° E in both the observed and simulated SSH composite fields when the simulated NRG intensity anomalies are larger than their one standard deviation (hereafter referred to as NRG positive; similarly, NRG negative refers to the composite when the intensity anomalies are more negative than the minus one standard deviation). Although the EKE is too high in the upstream KE region during the NRG negative phase and in the downstream KE region (east of 153° E) during the NRG positive phase, the model otherwise reasonably captures the observed spatial pattern of the EKE contrast associated with the NRG's intensity change. Specifically, the EKE in the upstream KE region decreases with the mean frontal strength; the EKE level west of 153° E is low (high) during the NRG positive (negative) phase. A similar negative correspondence between the regional EKE and the strength of the KE jet has been found in the altimeter observations (Qiu and Chen 2005, 2010).

4.2 Phase relationship between the EKE level and the intensity of RGs

In this section, the analysis on the phase relationship between the regional EKE and the intensity of the RGs is extended to cover the longer period from 1980 to 2007 than the altimeter observation period. Figure 7 compares the time series of the surface EKE (Fig. 7a), the middepth EKE at the depth of the 27.6σ_θ isopycnal (Fig. 7b), and the intensity anomalies of the NRG (Fig. 7c) and the SRG (Fig. 7d) along with that of the SSH-PC2. The surface EKE is computed based on the high pass-filtered surface geostrophic current velocities, while the middepth EKE is based on the filtered current velocities interpolated on the isopycnal depth. The temporal phase evolution of the EKE level is nearly identical between at the surface and at the middepth, both of which exhibit rather high-frequency variations whose time scales are typically several months (black lines in Fig. 7a, b). Although these high-frequency variations of the EKE level are not well correlated with the NRG or SRG intensity variation that has lower-frequency signals,

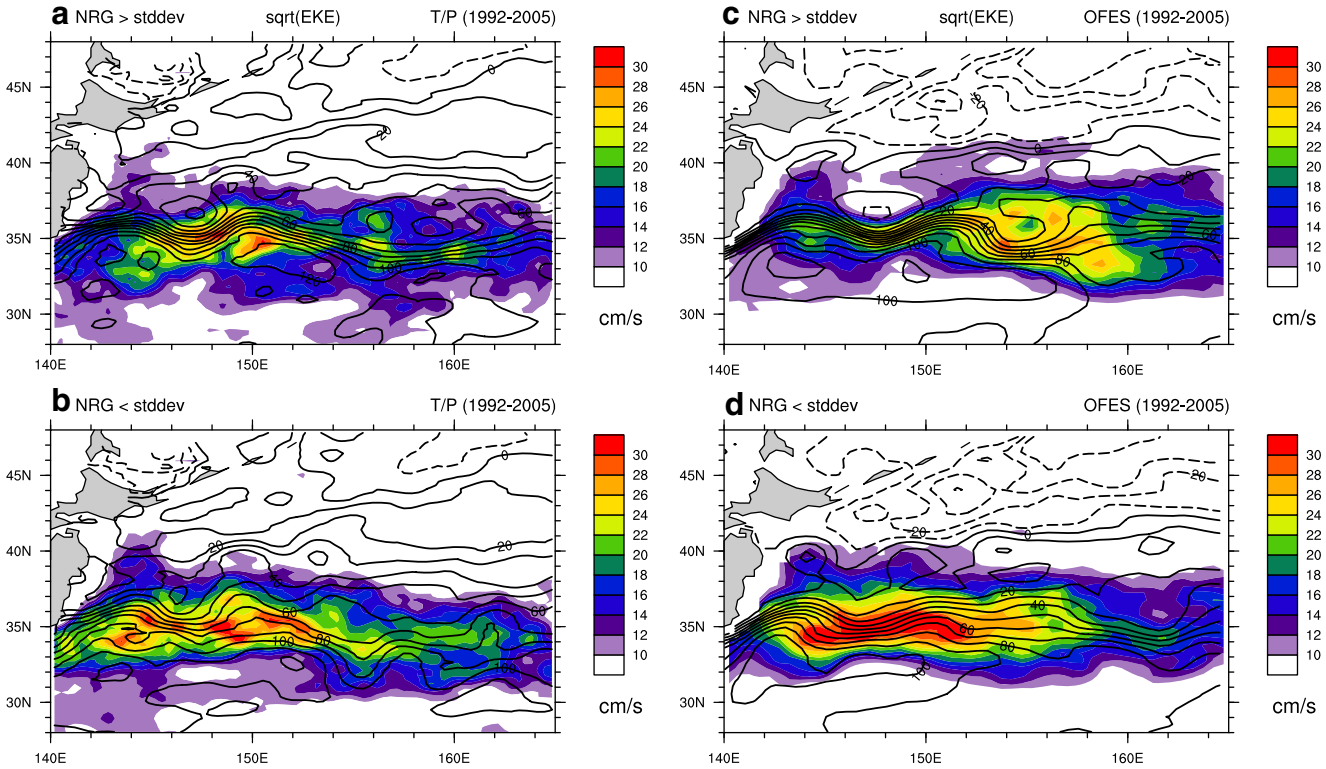

Fig. 6 Composite maps with respect to the NRG intensity of the square root of the EKE (*color shade*; units are in centimeters per second) and SSH (*black contours*; contour interval is 10 cm) based on the altimeter observations (**a**, **b**) and the OFES hindcast (**c**, **d**) during the altimeter observation era (1992–2005). A composite of the strong NRG (**a**, **c**) is defined as the averages of snapshots in which the NRG intensity is larger than its one standard deviation while the other weak NRG composite (**b**, **d**) is defined according to the NRG intensity less than one standard deviation

the EKE time series also display lower-frequency modulations (3-year low-pass filtered; red lines in Fig. 7a, b) on top of the mesoscale high-frequency variability.

The temporal phase relationship between the EKE level and the intensity of the RGs is better depicted in a lagged-correlation plot between the two time series with the 3-year low-pass filtering as shown for the NRG case in Fig. 8a. The lag is defined here to be positive when the EKE level leads the NRG intensity. The low-pass filtered EKE time series exhibits nearly simultaneous negative correlation (~ -0.5) with the low-pass filtered NRG intensity, which peaks when the former leads the latter by about 10 months (Fig. 8a). The statistical significance of the correlations is assessed based on a two-sided Student's t test. Degrees of freedom for the low-pass filtered time series of the NRG intensity are estimated to be 17 from their decorrelation time scales of 19 months and the total record length of 28 years. The negative correlation of the low-pass filtered time series between the EKE level and the NRG intensity is marginally significant at 95% confidence level (dotted line in Fig. 8a), while no significant correlation is found between the EKE level and the SRG intensity (not shown).

In their most recent analysis of the altimeter observations, Qiu and Chen (2010) noted the phase delay between the strengthened EKE level in the upstream KE region and the gradual build-up of the SRG. From the altimeter observations of the past 16 years, they argued that the period of a strong EKE level (1998–2001 in their Fig. 3b) preceded that of a strong SRG (2002–2005 in their Fig. 3d). This observed *positive* correlation and the ~4-year phase delay of the SRG intensity behind the EKE level is not captured in the OFES simulation. A solid understanding of the phase relationship between the RGs' intensity and the regional EKE level requires a longer observation record and a better simulation of the decadal modulations of the EKE level in the upstream KE region.

4.3 Relationship between the eddy modulation and the wind-forced large-scale circulation

In this section, we discuss what controls the low-frequency modulation of the simulated EKE level. Is

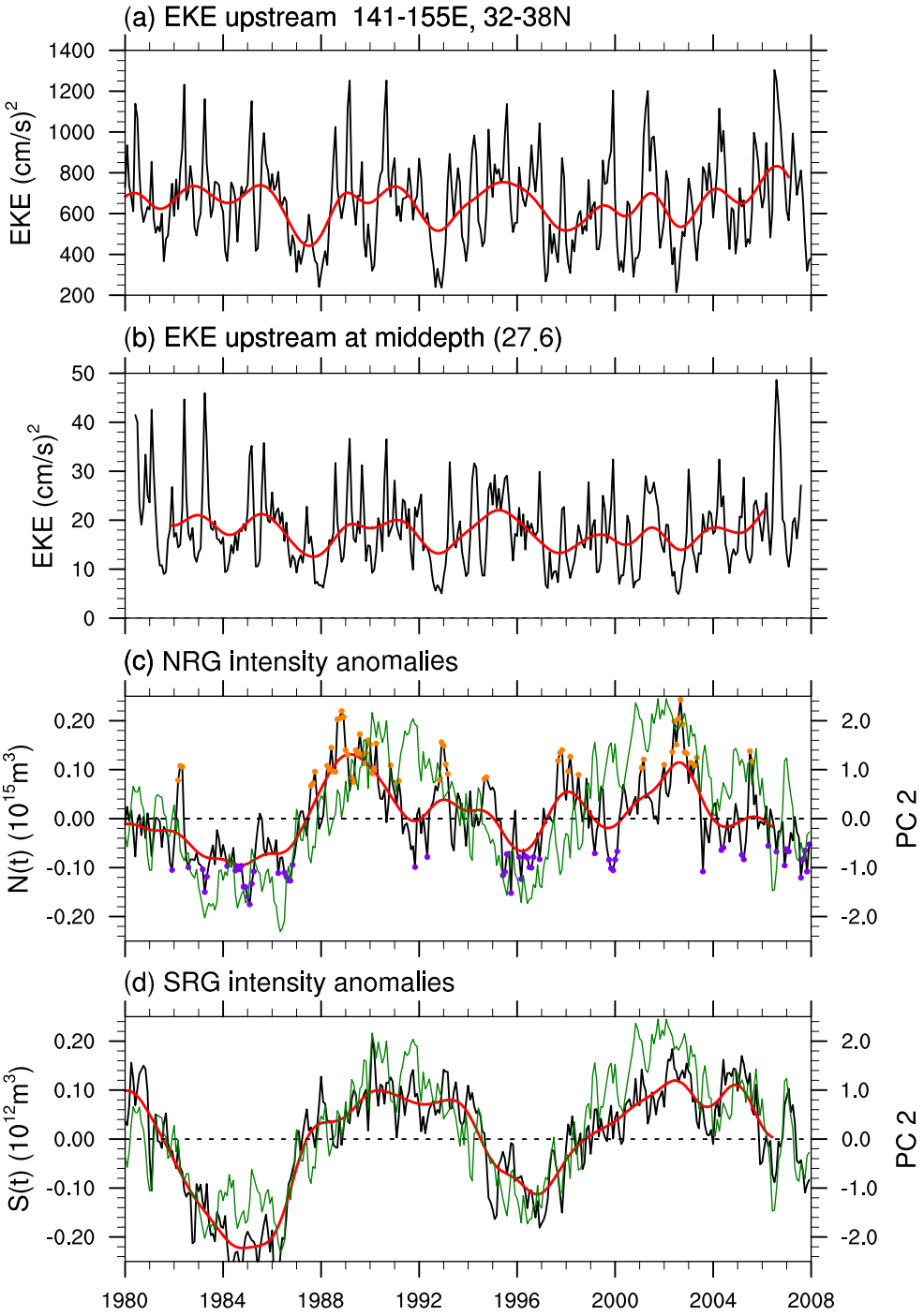

Fig. 7 Time series of the regional EKE level, **a** at the surface and **b** at middepth (on the isopycnal of 27.6σ_θ), averaged over the upstream KE region (32–38°N, 141–155° E). **c** Time series of the intensity anomalies of the NRG and **d** the SRG. *Black curves* are based on monthly mean while *red curves* indicate their 3-year low-pass filtered components. *Green curves* in **c** and **d** indicate time series of the second principal component of zonal mean SSH averaged over the KE region (142–180° E, SSH-PC2 of Taguchi et al. 2007). Seasonal cycles are removed from all the time series in **c** and **d**. *Orange (purple) dots* in **c** indicate the data points sampled for the strong (weak) NRG composites used in Fig. 4d, e. Units are in **a** and **b** cm^2 s^{-2}, **c** 10^{15} m^3, and **d** 10^{12} m^3

it still stochastic on interannual-to-decadal timescales or linked to the wind variations via the responding large-scale circulation changes? To examine the origin of the low-frequency EKE modulations, lagged-regression maps of the EKE levels onto the SSH-PC2 are constructed for the period from 1960 to 2007 (Fig. 9). The SSH-PC2 here can be regarded as a reference time series of the variation of the large-scale circulations in the KE region induced by wind variations in the North Pacific basin (see Section 3) and has been shown to lag behind the North Pacific Gyre Oscillation index, an oceanic expression of the atmospheric forcing associated with the North Pacific Oscillation (Di Lorenzo and coauthors 2008) by 2–3 years due to oceanic Rossby wave dynamics (Ceballos et al. 2009). Hence, the lagged-regression maps depict EKE evolutions in the KE region associated with the incoming, westward-propagating Rossby wave signals

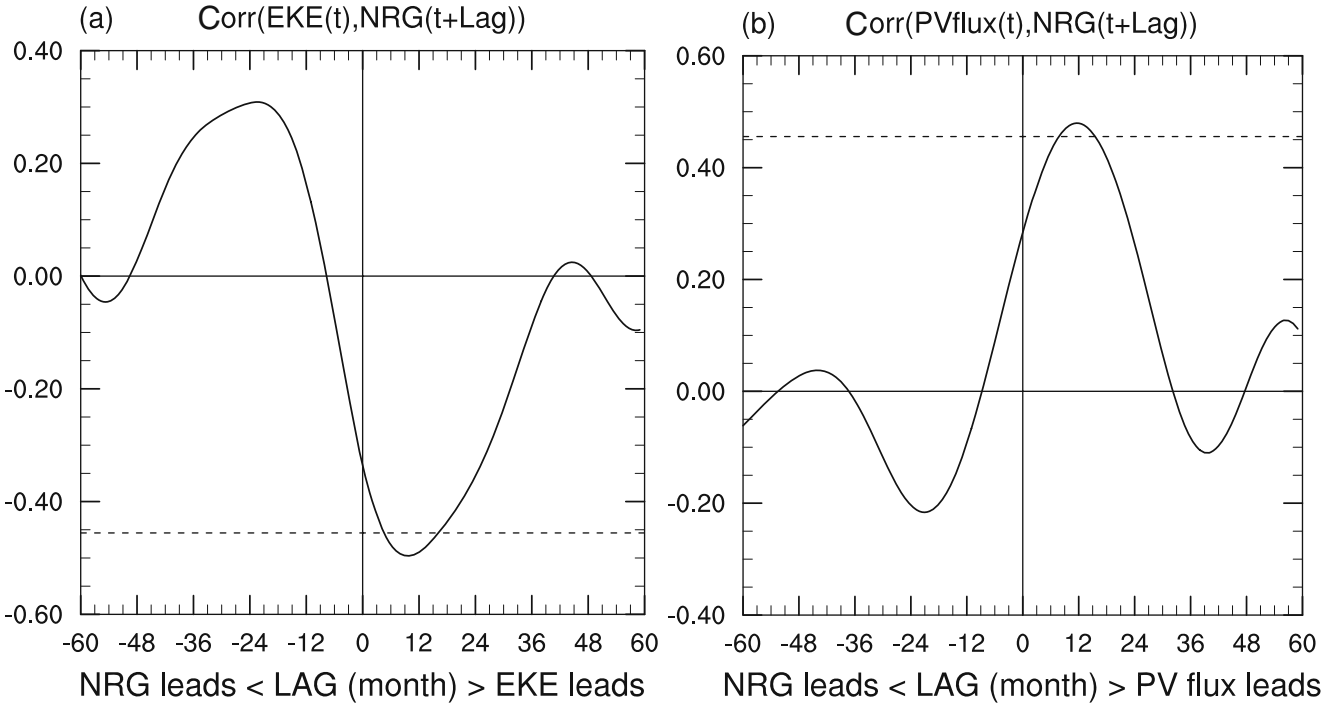

Fig. 8 **a** Lagged correlation between the regionally averaged EKE in the upstream KE region (32–38°N, 141–155° E) and the NRG intensity. The sign is defined as positive when the EKE leads the NRG. The correlation is based on low-pass filtered time series with half cutoff period of 3 years. **b** Same as **a** but for the correlation between the NRG intensity and the eddy PV flux convergence averaged over the NRG (34–38°N, 141–155° E). *Horizonal dotted lines* indicate statistically significant correlation limits with 95% confidene level

of the large-scale ocean circulation changes from the central-to-eastern Pacific. As the SSH-PC2 and the NRG intensity are overall correlated each other ($r = 0.58$; Fig. 2e), the regression of EKE level at lag 0 represents, to a large degree, the difference in the EKE level between the NRG positive and negative phases (Fig. 6c, d). The 0-lag EKE regression displays the reduced EKE levels in the upstream KE region and enhanced EKE levels in the downstream region, although the latter one is likely overemphasized in light of the model's EKE bias during the altimeter observation period (Section 4.1; Fig. 6). The regression maps at lags from −2 to 0 year reveal that the increased EKE signals come from the east and are associated with enhanced anticyclonic circulation to the south of the KE (positive SSHA shown in contours) and cyclonic circulation to the north, indicative of the wind-forced large-scale circulation changes triggering the EKE modulation in the downstream KE region. The enhanced EKE signals further propagate westward and elevate the EKE level in the upstream KE region at around lag 3 years.

Besides the influence of the strengthening of the KE jet, Qiu and Chen (2010) argued that the enhanced EKE signals in the upstream KE region could originate from the interaction between the southward migrating deep KE jet and the shallow topography of the Shatsky Rise located around 158–161° E. In the OFES simulation, however, such correspondence is not as obvious as observed (not shown), presumably because of the model bias in simulating the KE path around the Shatsky Rise (155–160° E). Specifically, the model fails to simulate the KE's mean path that deflects southward downstream of the second crest of the KE's quasi-stationary meanders around 154° E (Fig. 1a and Fig. 1a in Qiu and Chen 2010 for comparison), thereby the KE jet tends to flow at around 35∼36° N, further north than observed. This KE path bias may be a reason for the overestimated EKE level just west of Shatsky Rise (Fig. 6c, d), where the northerly KE jet overly

Fig. 9 Lagged regressions onto the second principal component ▶ of zonal mean SSH averaged over the KE region (142–180° E, SSH-PC2 of Taguchi et al. (2007) of square root of EKE (*color shade*; units in *color bar at the bottom* is centimeters per second) and SSH anomalies (*contours*; the contour interval is 10 cm; negative contours are *dotted*) for the period 1960–2007. Positive lags indicate that the SSH-PC2 leads the EKE. The SSH-PC2, EKE, and SSH are all applied 3-year low-pass filtering after removing seasonal signals to highlight low-frequency variations. Total SSH of 50 cm, indicating the axis of the KE, is superposed with a *green contour*

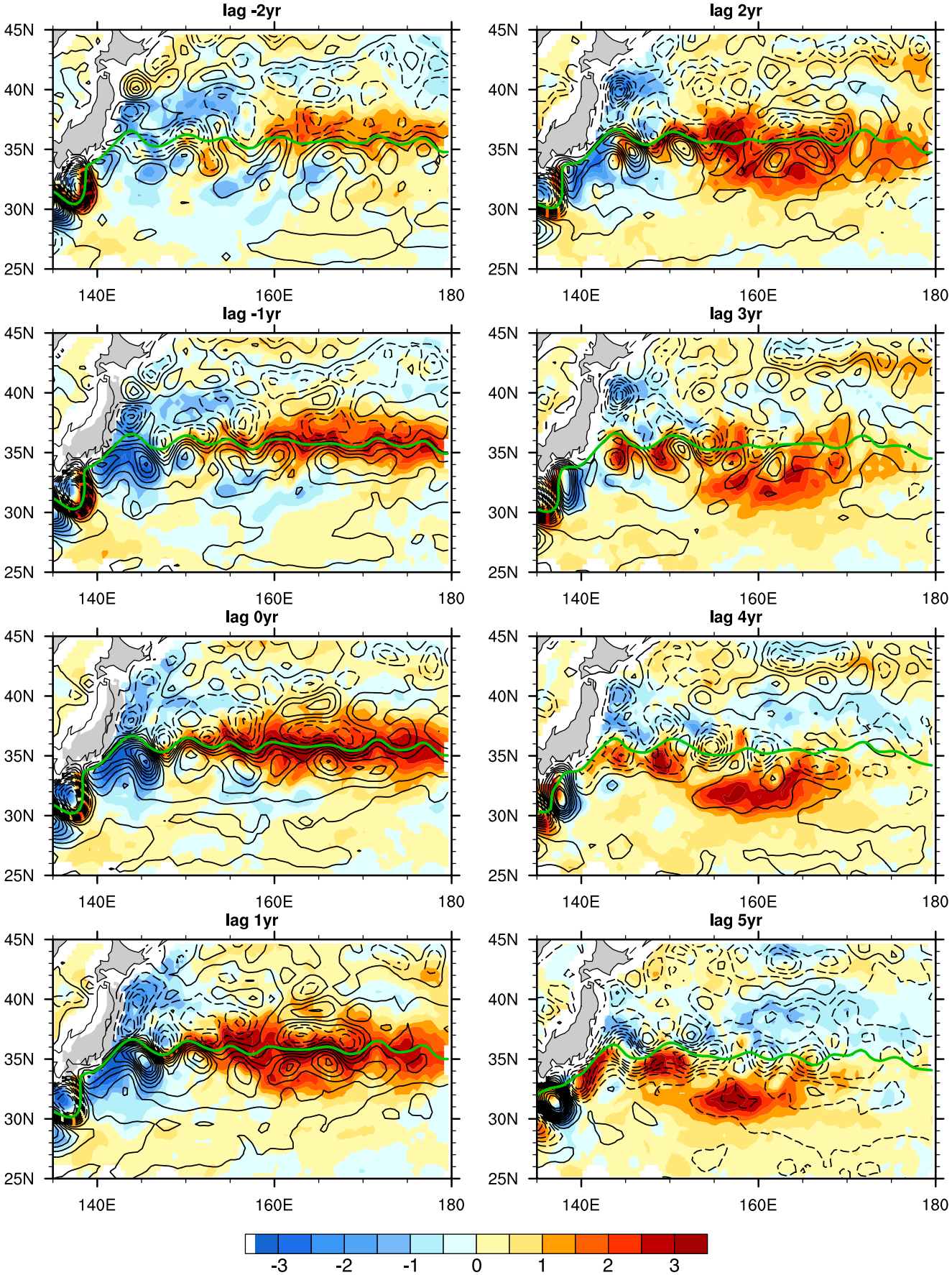

interacts with a shallow topography north of 35° N. The evolution of the EKE level in the upstream KE region may also be influenced by the meandering variations of the upstream Kuroshio south of Japan, which appears to have more stochastic components than in the downstream KE region in the OFES simulation.

5 Eddy feedback on composite time-mean recirculation gyres

One hypothesis that links the interannually modulating EKE level to the variability of the NRG intensity is that the eddy forcing associated with the former causes the latter. By performing the PV budget analysis using the OFES hindcast output, Qiu et al. (2008) have demonstrated that the convergent eddy PV fluxes are a primary driving mechanism for the time-mean NRG at middepth. In this section, we explore the role of the time-varying eddy forcing in the generation of the bimodal states of the NRG. Specifically, we apply the eddy PV flux analysis to each of the NRG bimodal states separately and examine whether circulations at middepth inferred from the convergent eddy PV fluxes could explain the simulated contrast associated with the NRG intensity change.

Following Qiu et al. (2008), we assume the PV balance given by the turbulent Sverdrup balance (Rhines and Holland 1979) on the isopycnal at middepth for each bimodal state.

$$\bar{\mathbf{u}} \times \nabla \overline{Q} \simeq -\nabla \times (\overline{\mathbf{u}' Q'}) \tag{7}$$

where the perturbations of PV and velocities are calculated from the three daily model output from 1980 to

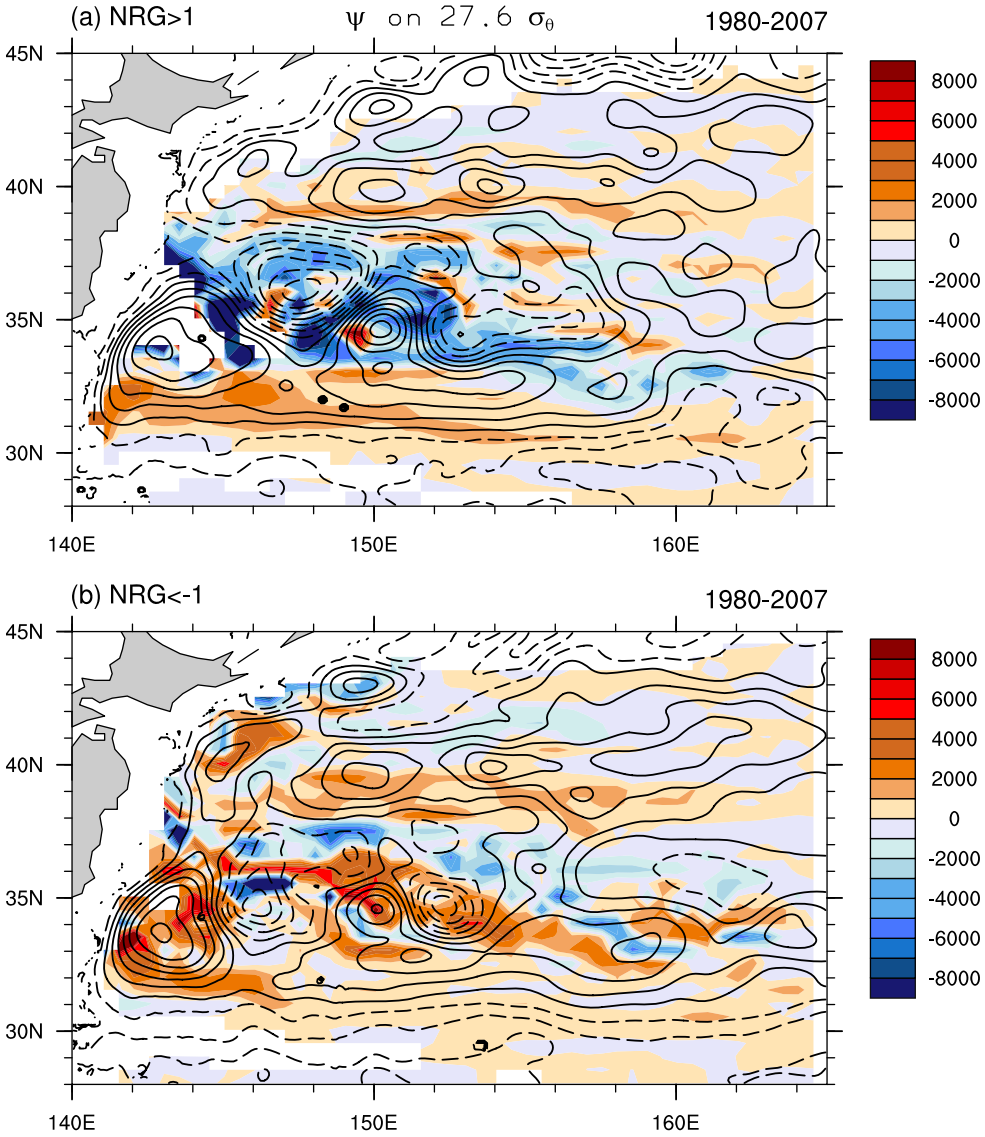

Fig. 10 Composite maps with respect to the NRG intensity of the the middepth stream function on the isopycnal of $27.6\sigma_\theta$ based on the OFES hindcast (*contours*; contour interval is 1,000 $m^2\ s^{-1}$) and that based on the estimate by turbulent Sverdrup balance from convergent eddy PV flux (*color shade*), during the period from 1980 to 2007. A composite of the strong NRG (**a**) is defined as the averages of snapshots in which the NRG intensity is larger than its one standard deviation while the other weak NRG composite (**b**) is defined according to the NRG intensity less than minus one standard deviation

2007 and derived by applying a high-pass filter with the half power cutoff period of 300 days. In other words, the perturbations here are defined relative to the slowly modulating background fields whose periods are longer than 300 days. Note that composite averaging with respect to the NRG intensity, rather than the time mean, is denoted by overbars in Eq. 7, as we are interested in impacts of eddies for the bimodal states of the NRG separately. The validity of this approach will be discussed later in this section. The spatial distribution of the composite eddy PV flux convergence is generally noisy by itself (not shown). Here, we attempt to translate the convergent eddy PV fluxes into integrated stream functions. Rescaling with the arc length p along constant $\overline{Q}$ contours, defined by $\partial|\mathbf{x}|/\partial p = |\nabla\overline{Q}|$ where $\mathbf{x}$ is the position of a fluid particle along the constant $\overline{Q}$ contours (Rhines and Holland 1979), Eq. 7 can be expressed as

$$\frac{\partial\overline{\Psi}}{\partial p} = -\nabla\times(\overline{\mathbf{u}'Q'}) \tag{8}$$

The instantaneous (three daily) convergent eddy PV fluxes are first composite-averaged with criteria of one standard deviation of the NRG intensity (the rhs of Eq. 8). The composite averaging here can be considered as the combination of the time averaging over a period when an individual NRG's extreme event exceeds the criterion and the ensemble averages of all events. Then, the composite mean eddy PV flux convergences are integrated pseudowestward along the constant $\overline{Q}$ contours from $p = 0$ along 165° E, yielding the stream function $\overline{\Psi}$ that is inferred from the turbulent Sverdrup balance. Figure 10 displays the composite mean stream functions on the isopycnal of $27.6\sigma_\theta$ derived from the simulated velocities interpolated on the isopycnal (contours) and inferred by the turbulent Sverdrup balance (color shade) for the NRG positive (Fig. 10a) and negative phases (Fig. 10b). The comparison between the simulated and inferred stream functions reveals that the turbulent Sverdrup balance assumed separately for the bimodal NRG states explains well the simulated spatial contrast associated with the NRG strength. Namely, the inferred stream function for the NRG positive phase (Fig. 10a color) indicates a cyclonic eddy PV flux forcing (bluish color) reaching $\overline{\Psi}$ value down to $-8{,}000\ \mathrm{m^2\ s^{-1}}$ in the region centered around 37° N, 147.5° E where the simulated NRG is indeed located. The cyclonic forcing is far less obvious in the inferred stream function for the NRG negative phase (Fig. 10b color). Note that the minimum $\overline{\Psi}$ value in the NRG during its positive phase is even smaller (larger amplitude) than that in the simulated NRG with $\overline{\Psi} \simeq -7{,}000\ \mathrm{m^2\ s^{-1}}$ at smallest. This indicates that the turbulent Sverdrup balance is not exact and other terms such as dissipation must play a role in the exact PV balance as shown by Qiu et al. (2008) for the time-mean NRG. It is also interesting to note that the anticyclonic circulation in the first crest of the KE's quasistationary meanders is enhanced during the NRG negative phase (bottom, contours), which is also suggested to be eddy-driven by the corresponding anticyclonic forcing in the inferred stream function (bottom, color shade). It has been suggested that the SRG variations also have an eddy-driven component (Qiu and Chen 2010).

Different from the study by Qiu et al. (2008) who investigated eddy's impact on the *time-mean* circulation

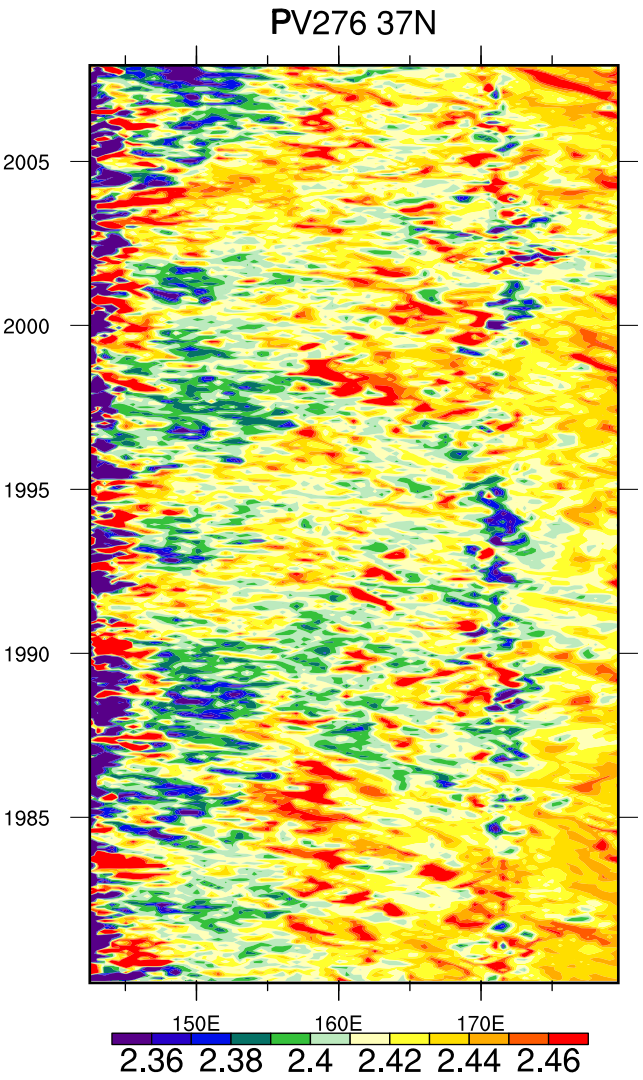

Fig. 11 Time-longitude section of the middepth PV on the isopycnal of $27.6\sigma_\theta$ along 37° N for the period from 1980 to 2007. Units are in $10^{-11}\ \mathrm{m^{-1}\ s^{-1}}$

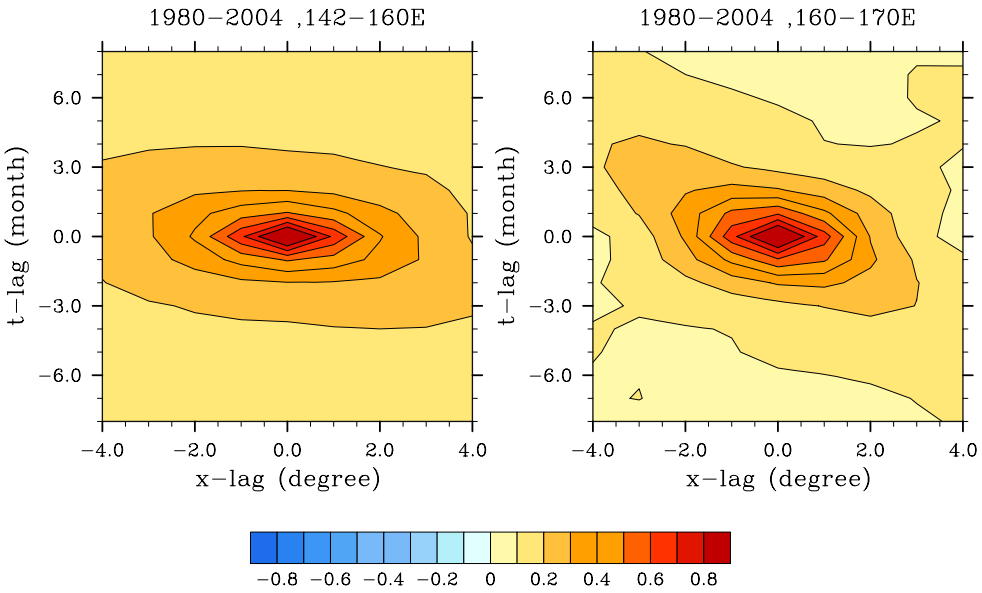

Fig. 12 Longitude-time lag correlation of the middepth PV on the isopycnal of 27.6σ_θ along 37° N for the period from 1980 to 2004 for the longitudinal sectors of 142–160° E (*left*; upstream) and 160–180° E (*right*; downstream)

using the PV balance characterized by the turbulent Sverdrup balance, we assumed the PV balance separately for the *composite* means of the NRG bimodal states. Since the turbulent Sverdrup balance (Eq. 7) should hold in a steady state after all transient adjustments are completed, there is a time scale issue for the present composite approach to be valid. Specifically, the time scale τ_{adj} for the PV signals to propagate from its source region to the center longitude of the NRG should be much shorter than the time scale for the NRG modulation τ_{NRG}:

$$\tau_{\text{adj}} << \tau_{\text{NRG}}. \tag{9}$$

To evaluate the adjustment time scale τ_{adj}, the simulated PV anomalies on 27.6σ_θ are plotted as a function of time and longitude along 37° N (Fig. 11). PV signal propagation is overall westward with a slower phase speed in the downstream (east of 160° E) than the upstream KE region (west of 160° E). The former is possibly due to wind-forced Rossby waves, while the latter due to westward-moving mesoscale anomalies emanating from the unstable KE jet (Hogg 1988). The adjustment time scale for the turbulent Sverdrup balance is the time required for the PV anomalies to traverse from east to west. To better quantify the PV propagations, we construct 2D lagged correlation maps in space and time for the PV anomalies (Fig. 12; e.g., Qiu et al. 1991). A visual inspection of the slope in the 2D correlation map yields the phase speed $C_{\text{ph}} \simeq$ 4°/[1∼2 months] and 4°/[2∼3 months] in the upstream and downstream KE region, respectively. It is difficult, however, to identify source regions for the PV anomalies from the time-longitudinal section (Fig. 11). We test the sensitivity to the choice of the eastern boundary by setting it at 158° E just west of the Shatsky Rise and repeating the turbulent Sverdrup integration. The integration reproduces a nearly identical stream function field to that estimated with the eastern boundary set along 165° E (not shown), indicating that the NRG is driven by eddy PV fluxe convergence west of the Shatsky Rise and is independent of the eddy fluxes further to the east. Therefore, we assume here that the longitudinal distance that the PV anomalies have to transverse across be the distance between the center of the NRG (147.5° E) and the Shatsky Rise (159.5° E). In this case, the adjustment time scale τ_{adj} is estimated to be 3∼9 months, which is much shorter than τ_{NRG}, assuring that our composite turbulent Sverdrup balance approach is valid.

Lastly, the control of the convergent eddy PV fluxes on the NRG intensity modulation can be seen not only in the composite analysis but also in a lagged correlation between the NRG intensity and the area-mean convergent eddy PV fluxes (Fig. 8b). The NRG intensity is positively correlated, at lag about 10 months, with the convergent eddy PV fluxes averaged over a region where the NRG is distinct (34–38°N, 141–155° E), indicative of the eddy PV flux forcing causing the NRG intensity modulation. It is, however, unknown what determines the time lag of 10 months.

6 Summary and discussion

The multidecadal OFES hindcast simulation is analyzed to investigate the low-frequency variations of the

two recirculation gyres present respectively to the north and south of the KE jet and their relationship with the modulations and forcings of mesoscale eddies. A particular focus is placed on the northern recirculation gyre, which has recently been detected at middepth by the profiling float and moored current meter observations. The intensities of both the simulated recirculation gyres exhibit pronounced interannual-to-decadal variations particularly during the period after 1980. These intensity variations of the KE recirculation gyres are overall highly correlated with the second principal component of the zonal mean SSH averaged over the KE region (SSH-PC2; Fig. 2e), indicating that their temporal variations are largely controlled by the wind-forced large-scale circulation change. The change in spatial patterns associated with the NRG intensity is characterized by a well-defined (less distinct) NRG, faster (weaker) KE jet, and elongated (contracted) KE's quasistationary meanders during its strong (weak) phase. The well-defined NRG is also discernible in the SSH composite for the strong NRG phase in both the simulation and altimeter observations (Fig. 6 contours).

The simulated EKE is compared with altimeter observations for the period from 1992 to 2007. Although the simulated EKE time series averaged over the upstream KE region does not agree well with the observed on their phase evolution, the frequency and the amplitude of the EKE modulations are comparable between the model and the observations (Fig. 5a). Composite analysis demonstrates that the model reasonably captures the observed spatial patterns of the EKE change associated with the NRG's intensity; the EKE in the upstream KE region decreases with the NRG intensity or the mean frontal strength (Fig. 6 shade), consistent with the finding previously noted by Qiu and Chen (2005).

Further analysis of the simulated eddy fields suggests that the modulating mesoscale eddy activity has a significant influence on the low-frequency modulation of the NRG intensity. We extend the method used by Qiu et al. (2008) and quantify the eddy's influence on the composited mean flow fields. Assuming the turbulent Sverdrup balance, mean circulations induced by the convergent eddy PV fluxes are estimated separately for the bimodal (strong and weak) NRG states. The composite approach reveals that the change in the simulated NRG intensity is well explained by that in the stream function inferred from the turbulent Sverdrup balance, indicative of the eddy feedback modulating the low-frequency NRG intensity variations at middepth (Fig. 10).

Although we focused on the role of the mesoscale eddies in modulating the RGs at depth, our results do not necessarily exclude other possible mechanisms that could modulate the recirculation gyres. For example, from a series of high-resolution semi-idealized OGCM experiments, Nakano et al. (2008) argued that the generation of the high PV anomalies in the subinertial layer along the western boundary and subsequent offshore advection of the high PV anomalies are crucial for the formation of the *mean relative* NRG in the upper thermocline. Such high PV anomalies are also found in the OFES hindcast simulation advecting from the eastern slope of the Izu Ridge to a region to the north of the KE jet in the upper thermocline (M. Nonaka, in preparation).

The existence of the NRG could play an important role in locating the mean KE jet as it is observed around 35° N, a few degrees southward to the subtropical–subarctic gyre boundary in the Sverdrup circulations; the NRG blocks the Kuroshio current that would otherwise overshoot further north and causes its separation from the Japan coast by creating an adverse pressure gradient along the coast (Nakano et al. 2008) or by creating an intergyre area commonly known as the mixed water region (Qiu et al. 2008). This study suggests that the NRG may also be a crucial agent to induce the low-frequency variability of the KE jet, especially for its intensity variations through the low-frequency eddy-driven modulation of the NRG intensity.

Acknowledgements The authors thank two anonymous reviewers for their careful reading that helped improve the earlier version of this manuscript. This work is supported by the Japan Agency for Marine-Earth Science and Technology (JAMSTEC). MN, BT, and HS are in part supported by the Agriculture, Forestry and Fisheries Research Council of Japan, through the research project POMAL (Population Outbreak of Marine Life); BT and MN are also supported by Japan Society for Promotion for Science, through a grant-in-aid for Scientific Research (C) 21540458. BQ and NS are supported by the US National Science Foundation (NSF) through Grant OCE-0220680 and Grant OCE06-47994, respectively. IPRC Publication Number 691 and SOEST Publication Number 7927.

References

Berloff P, Hogg A, Dewar W (2007) The turbulent oscillator: a mechanism of low-frequency variability of the wind-driven ocean gyres. J Phys Oceanogr 37:2363–2386

Ceballos L, Lorenzo ED, Hoyos C, Schneider N, Taguchi B (2009) North Pacific gyre oscillation synchronizes climate fluctuations in the eastern and western boundary systems. J Climate 22:5163–5174

Cessi PR, Ierley G, Young WR (1987) A model of inertial recirculation driven by potential vorticity anomalies. J Phys Oceanogr 17:1640–1652.

Deser C, Alexander MA, Timlin MS (1999) Evidence for a wind-driven intensification of the Kuroshio current extension from the 1970s to the 1980s. J Climate 12:1697–1706

Di Lorenzo E and coauthors (2008) North Pacific gyre oscillation links ocean climate and ecosystem change. Geophys Res Lett 35:1–6. doi:10.1029/2007GL032838

Dijkstra HA, Ghil M (2005) Low-frequency variability of the ocean circulation: a dynamical system approach. Rev Geophys 43:RG3002. doi:10.1029/2002RG000122

Ducet N, LeTraon P-Y, Reverdin G (2000) Global high resolution mapping of ocean circulation from TOPEX/Poseidon and ERS-1/2. J Geophys Res 105:19477–19498

Hogg N (1988) Stochastic wave radiation by the Gulf Stream. J Phys Oceangr 18:1687–1701.

Hogg AM, Killworth PD, Blundell JR, Dewar WK (2005) Mechanisms of decadal variability of the wind-driven ocean circulation. J Phys Oceanogr 35:512–531

Jayne S, Hogg N, Waterman S, Rainville L, Donohue K, Watts D, Tracey K, McClean J, Maltrud M, Qiu B, Chen S, Hacker P (2009) The Kuroshio extension and its recirculation gyres. Deep Sea Res 56:2088–2099

Jiang S, Jin F-F, Ghil M (1995) Multiple equilibria, periodic, and aperiodic solutions in a wind-driven, double-gyre, shallow-water model. J Phys Oceanogr 25:764–786

Kalnay E and coauthors (1996) The NCEP/NCAR 40-year reanalysis project. Bull Am Meteor Soc 77:437–471

Kwon Y-O, Deser C (2007) North Pacific decadal variability in the community climate system model version 2. J Climate 20:2416–2433

Masumoto Y, Sasaki H, Kagimoto T, Komori N, Ishida A, Sasai Y, Miyama T, Motoi T, Mitsudera H, Takahashi K, Sakuma H, Yamagata T (2004) A fifty-year eddy-resolving simulation of the world ocean—preliminary outcomes of OFES (OGCM for the earth simulator). J Earth Simul 1:31–52

Maximenko N, Niiler P (2004) Hybrid decade-mean global sea level with mesoscale resolution. In: Saxena N (ed) Recent advances in marine science and technology. PACON International, Honolulu, pp 55–59

McClean J, Jayne S, Maltrud M, Ivanova D (2009) The fidelity of ocean models with explicit eddies. In: Hecht MW, Hasumi H (eds) Ocean modeling in an eddying regime. Am Geophys Union Geophys Monograph, no 177. American Geophysical Union, Washington, pp 149–163

Miller A, Cayan D, White W (1998) A westward-intensified decadal change in the North Pacific thermocline and gyre-scale circulation. J Climate 11:3112–3127

Nakamura H, Sampe T, Tanimoto Y, Shimpo A (2004) Observed associations among storm tracks, jet streams, and midlatitude oceanic fronts. In: Wang C, Xie S-P, Carton J (eds) Earth climate: the ocean-atmosphere interaction. Amer. Geophys. Union. Geophys. Monograph, no 147. American Geophysical Union, Washington, pp 329–345

Nakano H, Tsujino H, Furue R (2008) The Kuroshio current system as the jet and twin "relative" recirculation gyres embedded in the Sverdrup circulation. Dynam Ocean Atmos 45:135–164

Niiler P, Maximenko N, McWilliams JC (2003a) Dynamically balanced absolute sea level of the global ocean derived from near-surface velocity observations. Geophys Res Lett 30:2164. doi:10.1029/2003GL018628

Niiler P, Maximenko N, Panteleev G, Yamagata T, Olson D (2003b) Near-surface dynamical structure of the Kuroshio extension. J Geophys Res 108:3193. doi:10.1029/2002JC001461

Nonaka M, Nakamura H, Tanimoto Y, Kagimoto T, Sasaki H (2006) Decadal variability in the Kuroshio–Oyashio extension simulated in an eddy-resolving OGCM. J Climate 19:1970–1989

Nonaka M, Nakamura H, Tanimoto Y, Kagimoto T, Sasaki H (2008) Interannual-to-decadal variability in the Oyashio Current and its influence on temperature in the subarctic frontal zone: an eddy-resolving OGCM simulation. J Climate 21:6283–6303

Pacanowski RC, Griffies SM (2000) MOM 3.0 manual. Technical report, Geophysical Fluid Dynamics Laboratory/National Oceanic and Atmospheric Administration, 680 pp

Pedlosky J (1996) Ocean circulation theory. Springer, Berlin

Pierini S, Dijkstra H (2009) Low-frequency variability of the Kuroshio extension. Nonlinear Process Geophys 16:665–675

Pierini S, Dijkstra H, Riccio A (2009) A nonlinear theory of the Kuroshio Extension bimodality. J Phys Oceanogr 39:2212–2229

Qiu B (2002) The Kuroshio Extension system: its large-scale variability and role in the midlatitude ocean–atmosphere interaction. J Oceanogr 58:57–75

Qiu B (2003) Kuroshio Extension variability and forcing of the Pacific decadal oscillations: responses and potential feedback. J Phys Oceanogr 33:2465–2482

Qiu B, Chen S (2005) Variability of the Kuroshio Extension jet, recirculation gyre and mesoscale eddies on decadal timescales. J Phys Oceanogr 35:2090–2103

Qiu B, Chen S (2010) Eddy-mean flow interaction in the decadally modulating Kuroshio Extension system. Deep Sea Res 57. doi:10.1016/j.dsr2.2008.11.036

Qiu B, Kelly K, Joyce T (1991) Mean flow and variability of the Kuroshio Extension from the Geosat altimetry data. J Geophys Res 96:18491–18507

Qiu B, Schneider N, Chen S (2007) Coupled decadal variability in the North Pacific: an observationally-constrained idealized model. J Climate 20:3602–3620

Qiu B, Chen S, Hacker P, Hogg N, Jayne S, Sasaki H (2008) The Kuroshio Extension northern recirculation gyre: profiling float measurements and forcing mechanism. J Phys Oceanogr 38:1764–1779

Rhines PB, Holland WR (1979) A theoretical discussion of eddy-driven mean flows. Dyn Atmos Oceans 3:289–325

Rosati A, Miyakoda K (1988) A general circulation model for upper ocean circulation. J Phys Oceanogr 18:1601–1620

Sasai Y, Sasaoka K, Sasaki H, Ishida A (2007) Seasonal and intraseasonal variability of chlorophyll-*a* in the North Pacific: model and satellite data. J Earth Simul 8:3–11

Sasaki H, Nonaka M, Masumoto Y, Sasai Y, Uehara H, Sakuma H (2008) An eddy-resolving hindcast simulation of the quasiglobal ocean from 1950 to 2003 on the Earth simulator. In: Hamilton K, Ohfuchi W (eds) High resolution numerical modelling of the atmosphere and ocean. Springer, New York, pp 157–185

Sasai Y, Richards KJ, Ishida A, Sasaki H (2010) Effects of mesoscale eddies on the marine ecosystem in the Kuroshio Extension region using an eddy-resolving coupled physical–biological model. Ocean Dyn. doi:10.1007/s10236-010-0264-8

Schneider N, Cornuelle BD (2005) The forcing of the Pacific decadal oscillation. J Climate 18:4355–4373

Schneider N, Miller A (2001) Predicting western North Pacific ocean climate. J Climate 14:3997–4002

Seager R, Kushnir Y, Naik NH, Cane MA, Miller J (2001) Wind-driven shifts in the latitude of the Kuroshio–Oyashio extension and generation of SST anomalies on decadal timescales. J Climate 14:4249–4265

Taguchi B, Xie S-P, Mitsudera H, Kubokawa A (2005) Response of the Kuroshio Extension to Rossby waves associated with

the 1970s climate regime shift in a high-resolution ocean model. J Climate 18:2979–2995

Taguchi B, Xie S-P, Schneider N, Nonaka M, Sasaki H, Sasai Y (2007) Decadal variability of the Kuroshio Extension: observations and an eddy-resolving model hindcast. J Climate 20:2357–2377

Taguchi B, Nakamura H, Nonaka M, Xie S-P (2009) Atmospheric influence of the Kuroshio/Oyashio extensions simulated for the 2003/4 winter in a regional atmospheric model. J Climate 22:6536–6560

Talley LD (1988) Potential vorticity distribution in the North Pacific. J Phys Oceanogr 18:89–106

Tokinaga H, Tanimoto Y, Xie S-P, Sampe T, Tomita H, Ichikawa H (2009) Ocean frontal effects on the vertical development of clouds over the western North Pacific: in situ and satellite observations. J Climate 22:4241–4260